Simulation of charge and exciton dynamics across nanostructured rough interfaces in organic light emitting devices

Giacomo Cotelli [1,2] Engin Torun [2,*] Stefano Gottardi [2] and Anna Köhler [1,3,†]

[1]*Soft Matter Optoelectronics, University of Bayreuth, 95440 Bayreuth, Germany*

[2]*Simbeyond B.V., Het Eeuwsel 57, 5612 AS Eindhoven, The Netherlands*

[3]*Bayreuth Institute of Macromolecular Research (BIMF), University of Bayreuth, 95440 Bayreuth, Germany*

(Received 20 May 2025; revised 3 July 2025; accepted 9 July 2025; published 29 July 2025)

In organic semiconductor devices, the deposition of organic layers may result in intermixed regions or rough interfaces between layers. To examine how roughness at organic-organic interfaces influences device performance, we conducted mesoscopic device simulations using a three-dimensional kinetic Monte Carlo algorithm. We simulated devices containing interfaces with periodic corrugation of either triangular or rectangular cross section. Our results show how the shape and size of interfacial roughness impacts on both charge and exciton dynamics of unipolar and bipolar devices. We first analyzed bilayer devices where the two layers are energetically offset. We find interfaces with triangular cross section display strong carrier funneling to the tips. This funneling translates to pronounced inhomogeneity in the spatial distribution of charge carriers, excitons, and excitonic losses. The tips act as injection hot spots, increasing the current density by up to two orders of magnitude, depending on the energy offset, compared to a flat-interface device. In contrast, the internal quantum efficiency of bipolar devices is surprisingly unaffected by interfacial morphology. In bipolar three-layer devices, we used this enhancement in current density to improve charge injection toward the central emissive layer. The recombination zone within the emissive layer can also be tuned through the configuration and size of the morphology.

DOI: 10.1103/36kq-7pvt

I. INTRODUCTION

During recent decades, organic light emitting diodes (OLEDs) have attracted increasing attention as innovative light sources for the display and lighting industry: high contrast, low energy consumption, and the possibility to fabricate transparent and flexible devices are among the strong points in favor of conventional LEDs. The manufacture of OLEDs from solution, as an alternative to the well-established vacuum-evaporation techniques, has recently seen intense development, owing to the possibility to exploit well-established industrial-scale printing technologies [1–6] on a virtually unlimited substrate size and with a promisingly low waste fraction, leading altogether to lower fabrication costs.

Nevertheless, in terms of performances, solution-processed OLEDs still lag behind their vacuum-evaporated counterparts [5–9] and the causes behind this are yet to be fully clarified. Morphological effects have been suggested to be at play: the higher performances of vacuum-deposited films have been associated with their better film quality, e.g., in terms of reduced component segregation or aggregation [10–12]. Films produced by vacuum evaporation are usually more homogeneously flat and more densely packed than the corresponding solution-processed films, producing sharp, flat interfaces between adjacent layers [13–15], although curiously, in rare occurrences, the opposite case of solution processing yielding better results than evaporation has also been reported [16,17]. A crucial aspect of OLED fabrication involves the deposition of subsequent layers: the complex, multilayered structures which represent the state of the art for vacuum-deposited devices prove yet a tough challenge for solution processing, as the coating of an upper layer may lead to the partial dissolution or swelling of the layer below, thereby creating an intermixed or corrugated interface [18–21].

The effect of such inhomogeneous interfaces has been rarely studied: several works have addressed, by indirect spectroscopic means, the diffusion of small molecules in a host (e.g., C_{60} in a polymer matrix, [22,23]) or the intermixing between adjacent layers under heating [24], reporting that layer interpenetration may proceed in both cases to a surprisingly large extent. Similarly, it is also well known that severe roughness may be present at the interface between electrodes and injection layers, especially when indium-tin oxide is used as the cathode [25,26]. Such inhomogeneity and the subsequent creation of pinholes has been suggested to reduce the lifetime of devices by locally shorting the circuit [25,27]. On the other hand, engineered interfaces have been suggested as means by which to improve light outcoupling [28], but they are often flattened out with a suitable interlayer before the active layers.

In terms of simulation studies, the topic of inhomogeneous interfaces between layers has been occasionally approached in the field of organic photovoltaics: for example, Buxton and

*Present address: Photovoltaic Materials and Devices, Delft University of Technology, Mekelweg 4, 2628 CD Delft, The Netherlands.

†Contact author: anna.koehler@uni-bayreuth.de

Published by the American Physical Society under the terms of the Creative Commons Attribution 4.0 International license. Further distribution of this work must maintain attribution to the author(s) and the published article's title, journal citation, and DOI.

Clarke [29] addressed the effects of a periodic, sinusoidal roughness at the interface between two materials via a 2D drift-diffusion model, while Watkins *et al.* [30] ran three-dimensional kinetic Monte Carlo simulations on bicomponent blends with varying degrees of intermixing. Such theoretical studies helped elucidate the working principles of a good bulk heterojunction, observing how phase separation influences the generation and diffusion of charge carriers in photovoltaic devices, therefore affecting device efficiency.

To this day, however, the field of organic light emitting devices (OLEDs) has not benefited from similar studies: in this work, we aim to address this issue with an analysis of the effects of interfacial inhomogeneity between adjacent layers via kinetic Monte Carlo simulations of ideal OLED devices of increasing complexity.

In Sec. II, an overview on the simulation methodology is provided, along with relevant parameters. In Sec. III A, we analyze the impact of inhomogeneous interfaces on charge transport in hole-only bilayer devices, while the corresponding bipolar devices are presented in Sec. III B to observe the effect of interfacial morphology on exciton dynamics and losses. These observations are translated in Sec. III C to three-layer devices containing two interfaces. Finally, in Sec. IV we present a unified picture on the effects of interfacial roughness on charge transport, discuss by extrapolation how morphological features on a larger length scale may impact the device behavior, and speculate on the possible role of roughness in aggravating device degradation under some conditions.

TABLE I. Simulation parameters employed in this study.

Parameter	Value
Lattice step	1 nm
Device area	100×100 nm^2
Temperature	293 K
Injection energy barrier	0.2 eV
Explicit Coulomb calculation cutoff distance[a]	10 nm
Charge hopping cutoff distance	Two neighbors
Excitonic neighbor cutoff distance	Four neighbors
Electronic disorder (IP/EA)	0.10 eV [46]
Excitonic disorder (S_1/T_1)	0.05 eV [37]
Singlet exciton binding energy	1.00 eV [47]
Triplet exciton binding energy	1.25 eV[b]
Förster radius (exciton transfer, $\Delta E < 0.5$ eV)	1.5 nm [36]
Förster radius (exciton transfer, $\Delta E \geqslant 0.5$ eV)	3.5 nm [36]
Förster radius (EPQ, EPA)	3.5 nm [36]
Miller-Abrahams or Dexter prefactor (nearest neighbor attempt rate)	3.33×10^{10} s^{-1} [46]
Miller-Abrahams or Dexter wave function decay length	0.3 nm [46]

[a]Chosen for performance as in Refs. [40,43].
[b]Chosen as 0.25 eV higher than the singlet binding energy.

II. METHODS

Three-dimensional kinetic Monte Carlo (3D kMC) simulations were performed using the commercial software BUMBLEBEE [31], which in earlier studies showed good agreement with experiment for a wide array of devices, including phosphorescent, fluorescent, thermally activated delayed fluorescent (TADF), and hyperfluorescent devices [32–39].

Devices are modeled as a collection of molecular sites arranged on a simple cubic grid, with periodic boundary conditions along the directions parallel to the electrodes. Each molecular site can host an electron, a hole, a singlet exciton, or a triplet exciton. Intermolecular charge transport in the hopping regime is described using a Miller-Abrahams-type rate [40]. Energetic disorder is described according to the Gaussian disorder model [41], assuming a spatially uncorrelated Gaussian density of states (DOS) centered on the material-specific ionization energy (IP) or electronic affinity (EA) value. Correlated disorder produces qualitatively similar results, favoring a more homogeneous charge distribution, similar to the effect of a smaller degree of uncorrelated disorder (see Fig. S4 in the Supplemental Material [42]). Injection layers are not explicitly modeled: instead, an energy barrier is placed at each injecting electrode. Coulomb interactions are explicitly calculated within a 10 nm cutoff radius from each charge carrier, while a layer average is employed for carriers outside the cutoff radius [43].

A hole and an electron sitting on the same molecular site generate an exciton, the spin of which is randomly determined with a singlet (S) to triplet (T) relative probability of 1:3, as prescribed by spin statistics. On-site exciton energies are again extracted from a spatially uncorrelated Gaussian DOS. Exciton dissociation is naturally included as a result of either charge carrier leaving the exciton site, incurring a supplementary energy cost equal to the exciton binding energy. Exciton diffusion and loss processes are explicitly modeled: diffusion results from an exciton transfer to a free site, while transfer to a site already occupied by a polaron or a second exciton, respectively, results in exciton-polaron quenching (EPQ) or exciton-exciton annihilation (EEA). Upon EPQ, the exciton is lost and only the polaron is left; upon EEA, the diffusing exciton is lost, while the remaining exciton may change its spin state in accordance with spin conservation: singlet-singlet annihilation (SSA) results in a singlet, triplet-singlet (TSA) and singlet-triplet annihilation (STA) result in a triplet, and triplet-triplet annihilation (TTA) results in a singlet (25%) or triplet (75%) exciton (high-energy quintet states are neglected). Exciton diffusion, quenching, and annihilation phenomena are introduced via both the Dexter and Förster mechanisms, respectively, with a dependency $k_D \propto e^{-r}$ and $k_F \propto r^{-6}$ on the distance r between the origin and destination site; only excitons with a nonzero radiative rate may be transferred via the Förster mechanism. A Miller-Abrahams-type factor accounts for the exciton energy difference between the origin and destination site.

General simulation parameters are indicated in Table I: this set of values, determined in previous studies, has proven to realistically describe charge transport and excitonic phenomena both in phosphorescent [32,34–36] and (hyper)fluorescent [37,39] devices. In the spirit of simulating ideal symmetric devices as described below, we assume equal mobility parameters for holes and electrons, differently from previous works

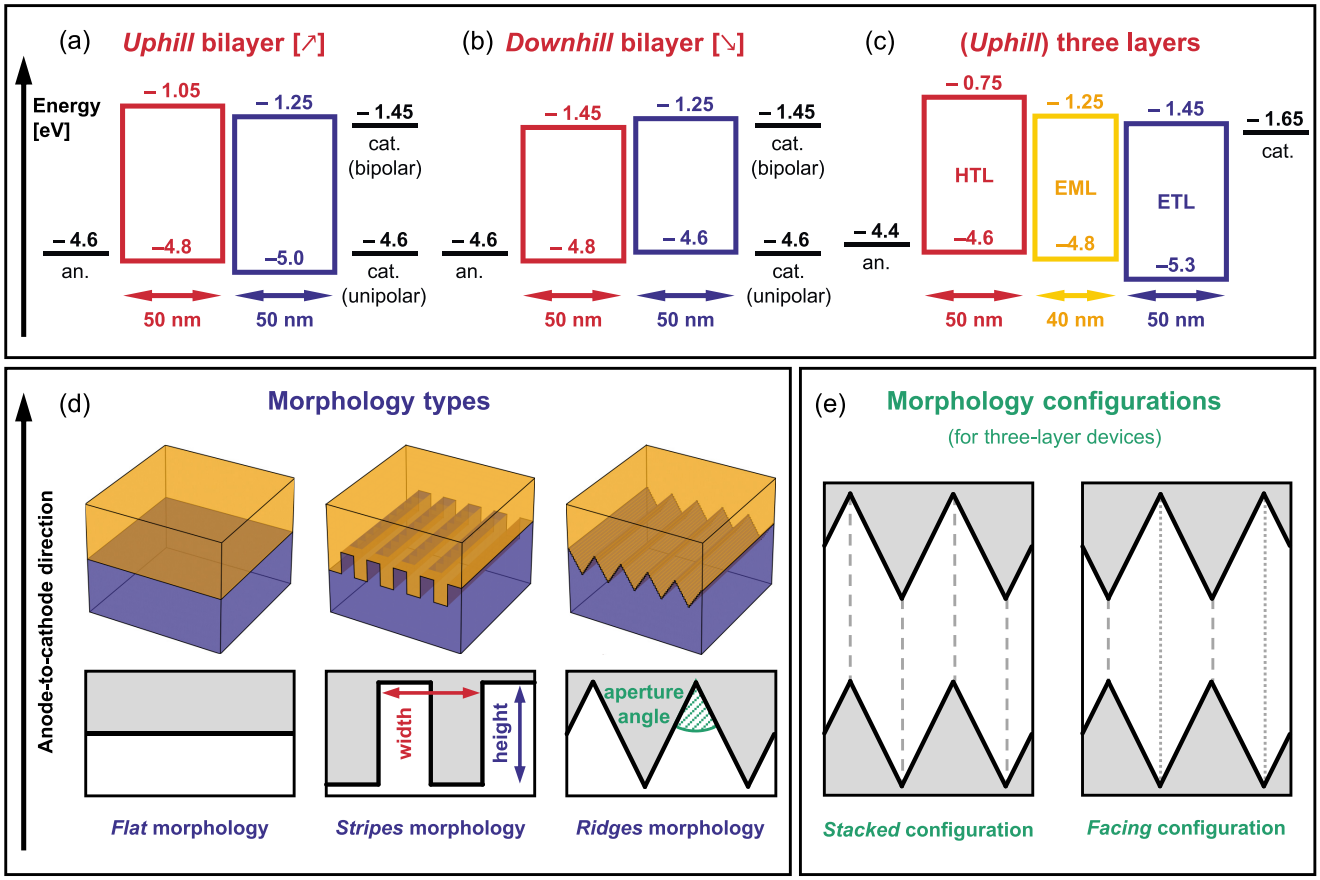

FIG. 1. Device schematics and morphology information. (a–c) Energy diagrams for the energetically and structurally symmetric devices simulated in this study: in the uphill bilayer structure (a), a +0.2 eV energy barrier is present across the interface in the direction of the applied field, representing an energy barrier for both types of charge carriers; in the downhill bilayer structure (b), the offset across the interface is −0.2 eV. Electrons are only present in bipolar devices, while unipolar devices are hole only. In the three-layer structure (c), a +0.2 eV energy barrier is present for either carrier type between its respective transport layer and the emissive layer (EML), and a +0.5 eV barrier between the EML and the opposite transport layer (double serving as a blocking layer). (d) Depictions of the interfacial morphologies studied in this work and (e) their possible configurations within three-layer devices.

[37]. Each simulation is run in five independent replicates corresponding to different disorder configurations.

Schematics for the bilayer and three-layer devices studied in this work are presented in Figs. 1(a)–1(c): to limit the complexity and the number of parameters to consider, the stacks are chosen as geometrically and energetically symmetric. We indicate as *uphill* (respectively, *downhill*) those devices in which charge carriers encounter a positive (respectively, negative) energy offset between adjacent layers in the direction of carrier drift. Material parameters, detailed in Table II, are comparable with common (fluorescent) transport materials. In bilayer devices, due to the symmetric choice of hole and electron energy levels, the two materials have the same exciton energy, so that no energy barrier for exciton diffusion is present across the interface.

Our devices are composed of two or three neat layers stacked between flat electrodes. To introduce roughness at the organic-organic interfaces, we attribute each site to a "material" according to the desired interface shape. The material determines the on-site electronic parameters (IP, EA) and on-site excitonic parameters (singlet or triplet energy, Förster or Dexter transfer rates). The "resolution" of the morphology is determined by the lattice step (1 nm).

To capture the basic physics of the system, we introduced periodic interfacial roughness with simple geometric features: namely, we report results for a reference *flat* morphology and two rough interfaces with periodic corrugation and either triangular (*ridges*) or rectangular (*stripes*) cross section, displayed in Fig. 1(d). Specifically, the ridges and stripes morphology corrugate along one axis parallel to the electrodes and have constant cross section along the other: we indicate as *width* the corrugation period (along a direction parallel to the electrodes) and as *height* the amplitude of the oscillation (along the anode-to-cathode direction). For the ridges morphology, we furthermore define an *aperture angle* $\alpha = 2 \times \arctan[\text{width}/(2 \times \text{height})]$.

Details on the calculation of current density, internal quantum efficiency, charge or exciton density [44], and event rates are given in Sec. S4 of the Supplemental Material [42]. Density maps displayed in the following sections were generated using the LIPARI color map from Ref. [45] as supplied in the CMCRAMERI module for PYTHON3.

TABLE II. Material parameters employed in this study.

	IP (eV)	EA (eV)	S_1 (eV)[a]	T_1 (eV)[a]	$k_{S,rad}$, $k_{T,IC}$(s^{-1})[b]
Uphill bilayers					
Hole transport layer	–4.80	–1.05	2.75	2.50	10^8, 10^4
Electron transport layer	–5.00[c]	–1.25	2.75	2.50	10^8, 10^4
Downhill bilayers					
Hole transport layer[d]	–4.80	–1.45	2.35	2.10	10^8, 10^4
Electron transport layer[d]	–4.60[e]	–1.25	2.35	2.10	10^8, 10^4
Uphill three layers					
Hole transport	–4.60	–0.75	2.85	2.60	0, 0
Electron transport	–5.30	–1.45	2.85	2.60	0, 0
Emissive layer	–4.80	–1.25	2.55	2.30	10^8, 10^4

[a]S1=EA-IP-(binding energy).
[b]Rate for the radiative decay from the singlet state and internal conversion from the triplet state; rates for (reverse) intersystem crossing, internal conversion from the singlet state, and radiative decay from the triplet state are zero.
[c]Lowered to −5.10, −5.20, −5.30 eV to test performances at increasing energy barrier in Fig. 4.
[d]Defined so as to obtain the same built-in voltage for uphill and downhill bipolar devices.
[e]Raised to −4.50, −4.40, −4.30 eV to test performances at increasing energy offset in Fig. 4.

III. RESULTS

A. Unipolar bilayers

We analyzed the effect of interfacial morphology on charge transport in unipolar (hole-only) bilayer devices [Fig. 1(a)]. In Fig. 2, we consider how differently shaped interfaces affect the spatial distribution of charges. Figure 3 reports the current voltage curve for representative devices. The impact of the energetic offset across the interface is addressed in Fig. 4.

Figure 2(a) presents the hole distribution at a modeled 6.0 V applied bias in uphill devices containing interfaces with various morphologies: a flat interface, three ridges interfaces with varying feature size, and a stripes interface. In all cases, holes injected from the anode [left electrode in Fig. 2(a)] trivially accumulate at the interface due to the IP difference between layers. The hole distribution at the interface is influenced by the morphology: in devices which contain a ridges morphology, charge carriers are funneled toward the convex tips of the interface, leading to an enhanced charge carrier density there, as compared to a stripes morphology [Fig. 2(b)]. As a result of this funneling, the tips act as injection points toward the adjacent layer, determining within it a spatially inhomogeneous hole distribution characterized by "plumes" of injected carriers. The areas between the tips are instead depleted from charges. This charge carrier funneling translates to an inhomogeneous, quasifilamentary current flow. The

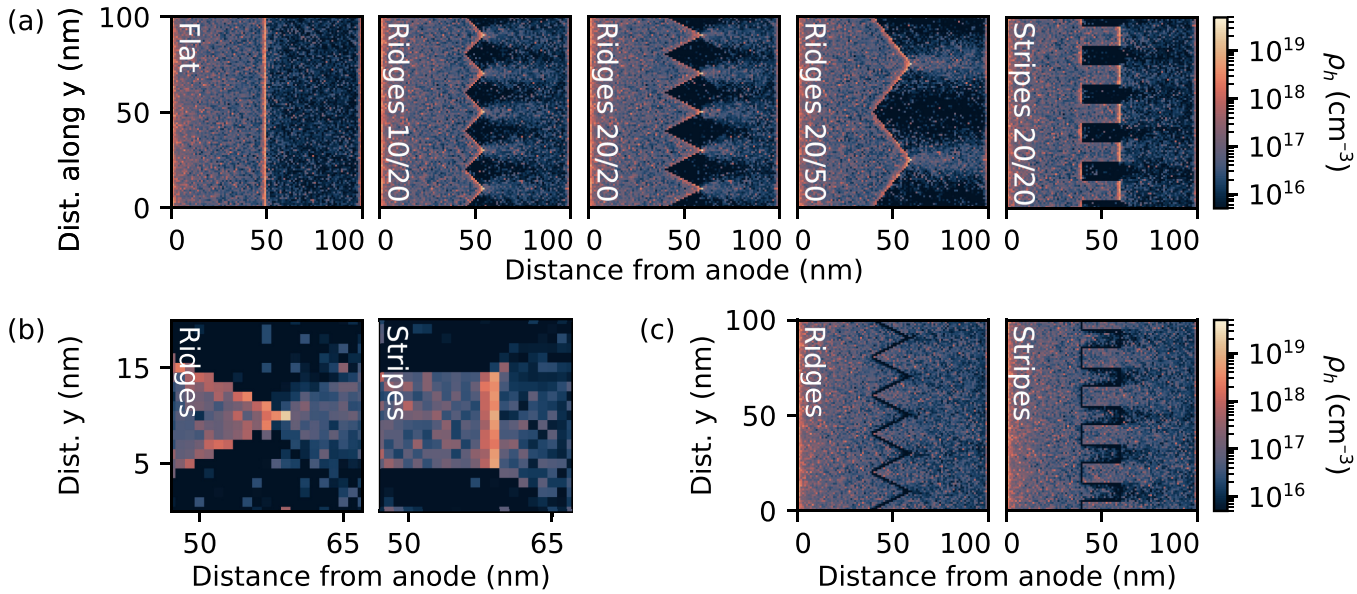

FIG. 2. Unipolar bilayers, heat maps. Charge-density maps at 6.0 V applied bias in (a) hole-only uphill bilayers with (left to right) a flat morphology, three ridges morphologies, and a stripes morphology. Feature size is indicated as height/width in nanometers. (b) Zoom-in on the tips of a ridges device and a stripes device at equal feature size (20 nm high, 20 nm wide). (c) Charge-density maps at 6.0 V applied bias in hole-only downhill bilayers with stripes or ridges morphology. In all figure parts, holes move from the left to the right.

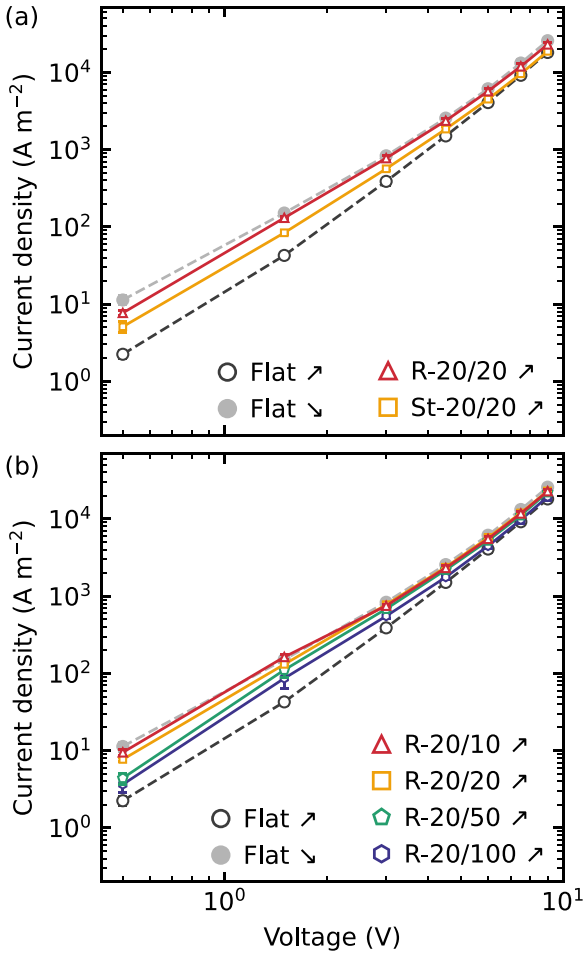

FIG. 3. Unipolar bilayers, current density. Current density vs voltage (*JV*) curves of devices containing (a) a ridges (△) or stripes (□) interface 20 nm wide, 20 nm high or (b) ridges interfaces with 20 nm high and increasing width (10 nm △, 20 nm □, 50 nm ⬠, 100 nm ⬡). Curves for flat uphill (◯) or downhill (●) devices are reported for reference. Uncertainty on the current density is smaller than the symbol size; lines are provided as a guide to the eye.

effect is significantly softened with a stripes morphology. The area between the stripes fingers is still depleted of charge density, but the injection occurs over the whole interfacial line in the direction of the electric field, as shown in the video in the Supplemental Material [42]. Correspondingly, there are no noticeable size effects (see Supplemental Material [42], Fig. S3). Finally, Fig. 2(c) compares the distribution of holes in downhill devices containing a ridges or stripes interface under a modeled 6.0 V applied bias. Both devices exhibit a charge-density gradient from anode to cathode and a carrier-depleted region at the interface, as charge carriers cannot hop back to the left-side layer. Aside from that, the interfacial morphology shows little effect on device properties (also see Fig. S3 in the Supplemental Material [42]).

Considering the *JV* curves of uphill devices at varying interfacial morphology for equal feature size [Fig. 3(a)], we observe a higher current density at any given voltage in the order ridges > stripes > flat. This effect is particularly strong at low voltages and for small aperture angles (Fig. 3(b) and

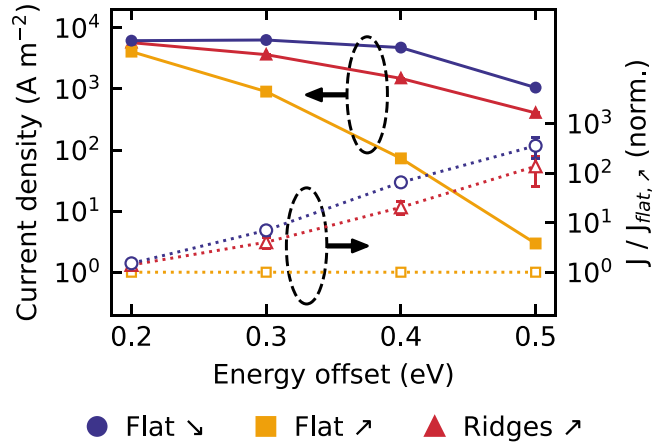

FIG. 4. Unipolar bilayers, effect of the energy offset. Current density at 6.0 V (filled markers) and relative current density compared to the uphill flat-interface device ($J_i/J_{\text{flat},\nearrow}$, empty markers) vs the energy offset across the interface for hole-only downhill (◯) and uphill (□) flat-interface bilayer devices, and for an uphill bilayer with a 20 nm high, 20 nm wide ridges interface (△). Uncertainty on the absolute current density is smaller than the symbol size; lines are provided as a guide to the eye.

Supplemental Material [42], Fig. S7(c)). In fact, it can render the current in the devices with a ridges interface close to that of a flat downhill device, implying that the energetic barrier becomes irrelevant, thus effectively improving charge injection through the interface. Such injection boost becomes even more relevant when a higher barrier is present at the interface. In Fig. 4 we compare the current density at 6.0 V for an uphill ridges device (20 nm high, 20 nm wide, red triangles) and a flat device (uphill and downhill) as a function of the energy offset across the interface. In the flat downhill device, the increasing energy offset produces an increasing extraction barrier at the cathode. Remarkably, the current density in the ridges devices is significantly higher (up to a factor of 100 for a 0.5 eV offset) compared to the flat uphill device. In fact, it becomes strikingly close to the current density of the barrierless flat downhill device. Hence, it is possible to use a ridges morphology to significantly boost charge injection across interfaces featuring a large energy barrier. This will be explored further for the case of a three-layer device in Sec. III C. Vice versa, consistently with previous observations on charge distribution, downhill devices show no influence of morphology on current density (see Fig. S7(b) in the Supplemental Material [42]).

B. Bipolar bilayers

In Fig. 5–7, we analyze the behavior of uphill bilayer devices containing ridges interfaces, and in which both electrons and holes are injected. We report the spatial distribution of holes, singlet excitons, and losses due to exciton-polaron quenching (EPQ) and exciton-exciton annihilation (EEA) (Fig. 5). We analyze which loss processes reduce the internal electroluminescence quantum efficiency (IQE) (Fig. 6), then compare devices with different ridges width (corrugation period) in terms of current density [Fig. 7(a)] and IQE [Fig. 7(b)]. We refer to the Supplemental Material [42]

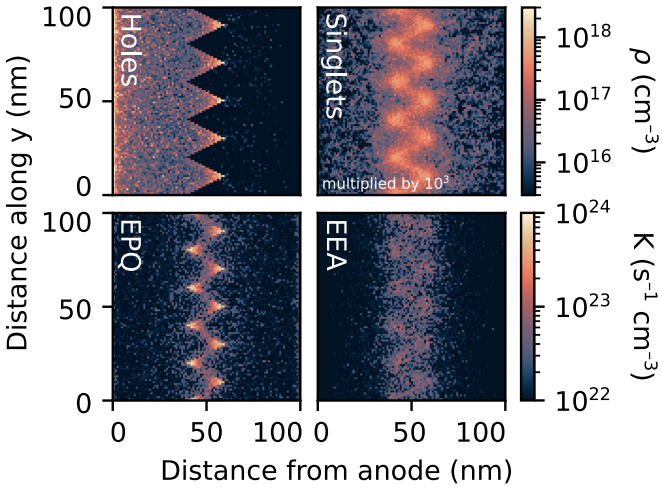

FIG. 5. Bipolar bilayers, density maps. Density maps for holes, singlets, exciton-polaron quenching (EPQ), and exciton-exciton annihilation (EEA) events in a bipolar bilayer device containing a ridges morphology 20 nm high, 20 nm wide, under 4.0 V applied bias. Holes move from left to right; electrons move from right to left. The energy barrier across the interface is +0.2 eV for both types of carriers; no barrier is present for excitons.

(Fig. S12) for a brief treatment of downhill devices which, as in unipolar devices, show little influence of the morphology on device behavior.

Figure 5 illustrates the distribution of holes, singlet excitons, and losses via EPQ or EEA in a device containing a 20 nm high, 20 nm wide ridges interface at 6.0 V. The hole distribution shows that, analogous to unipolar devices, carriers are funneled toward the tips of the interface (see Supplemental Material, Figs. S9–S11 [42] for electron distribution). Comparing the absolute values of hole density at the tips in the bipolar device (2×10^{18} cm^{-3}, i.e., 2×10^{-3} charges per site) and the analogous unipolar device (2×10^{19} cm^{-3}, i.e., 2×10^{-2} charges per site) shows that charge accumulation seems to be hindered by recombination at the interface. Notably, holes (Fig. 5, top left) and electrons (see Supplemental Material [42], Fig. S9) accumulate separately on alternate tips. The singlet density (Fig 5, top right) is highest around the tips of the morphology. The inner volume of each tip becomes a hot spot for EPQ losses (Fig. 5, bottom left) due to the high local charge density there. In contrast, EEA events (Fig. 5, bottom right) are more spread out, likely due to exciton diffusion.

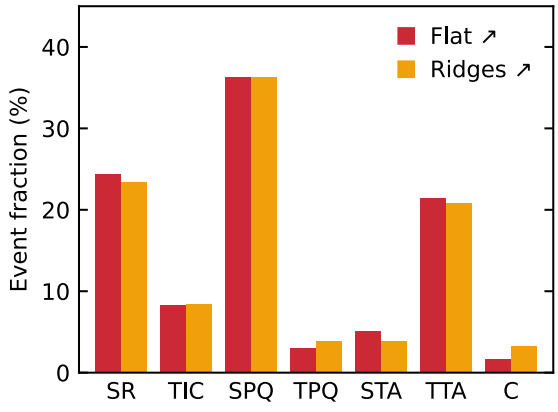

FIG. 6. Bipolar bilayers, loss processes. Comparison of excitonic events in uphill bipolar bilayers with either a flat or ridges (20 nm high, 20 nm wide) interface, under 4.0 V applied bias. Abbreviations: SR, singlet radiative decay; TIC, triplet internal conversion; SPQ (TPQ), singlet (triplet) polaron quenching; STA (TTA), singlet (triplet) triplet annihilation; C, collection of carriers at the opposite electrode.

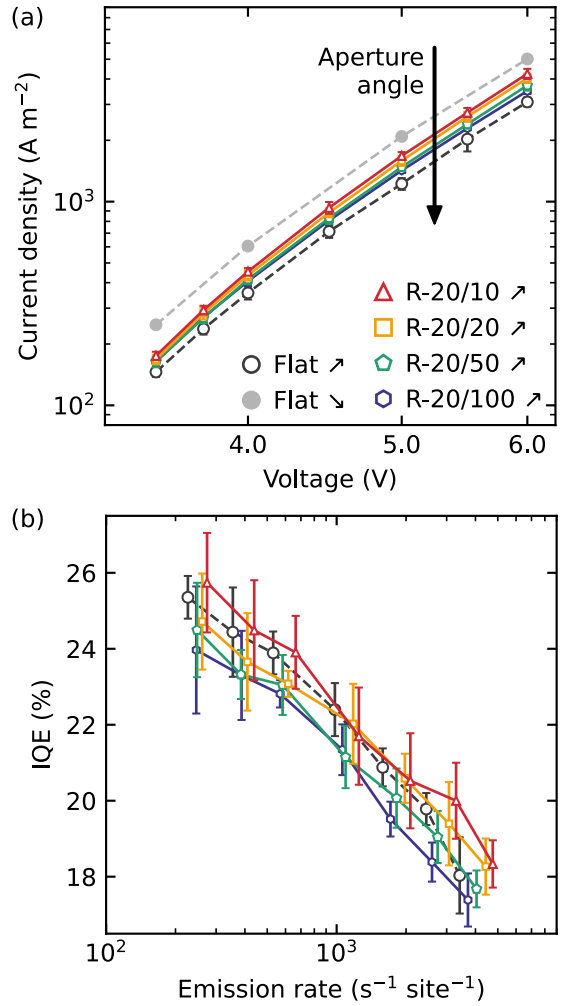

FIG. 7. Bipolar bilayers, current density, and efficiency. Comparison of (a) current density vs voltage and (b) IQE vs emission rate ($\propto$ luminance) between devices containing ridges interfaces 20 nm high with increasing width (10 nm △, 20 nm □, 50 nm ⬠, 100 nm ⬡). Curves for flat uphill (◯) or downhill (●) devices are reported for reference. Uncertainty on the absolute current density is smaller than the symbol size; lines are provided as a guide to the eye.

Analyzing in more detail reveals that the EPQ losses result mainly from singlet-polaron quenching (SPQ), whereas the EEA losses arise predominantly from triplet-triplet annihilation (TTA), as displayed in Fig. 6. In particular, Fig. 6 compares the fractions of radiative decay and nonradiative losses at 6.0 V for the ridges and flat devices. Despite the inhomogeneous spatial distribution of loss events in the ridges

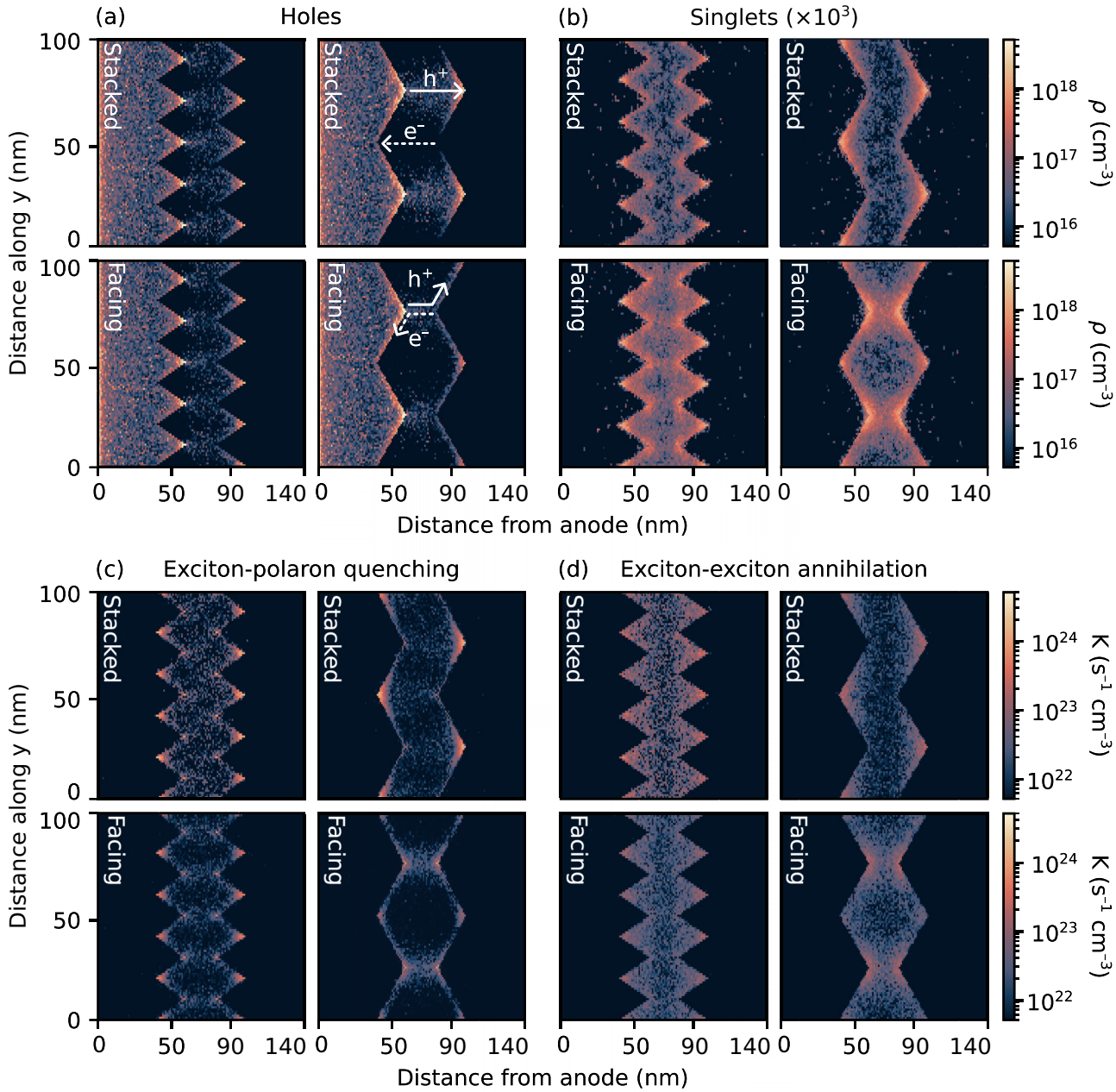

FIG. 8. Bipolar three layers, density maps. Density maps for (a) holes, (b) singlets, and (c) EPQ and (d) EEA events at 5.0 V for bipolar three-layer devices with ridges morphologies at varying size (in each panel, left: 20 nm high, 20 nm wide; right: 20 nm high, 50 nm wide) and offset (in each panel, top: stacked offset; bottom: facing offset).

device, its internal quantum efficiency (IQE) is strikingly close to that of the flat device (23%).

Figure 7(a) shows that, as in unipolar bilayers, bipolar ridges bilayers exhibit an increased current density compared to the flat uphill device; the current density also increases for narrower aperture angles, though the effect is weaker than for the unipolar bilayers. In fact, unlike in unipolar devices, bipolar ridges devices always show a lower current density compared to the flat downhill device. IQE [Fig. 7(b)] and IQE roll-off with luminance are not significantly affected by the interface shape or feature size, except for a minor drop in IQE at increasing width (see Supplemental Material [42], Sec. S6.3).

C. Bipolar three layers

In simulating three-layer devices, we have a double aim: firstly, to explore to which extent interfacial roughness may impact realistic devices and, secondly, to check whether a nanostructured interfacial morphology may be exploited to improve charge injection across an energy barrier, as suggested by the data of the unipolar bilayers.

We designed a simple three-layer structure [Fig. 1(c)] in which a pair of flat or ridges interfaces is placed between each transport layer (HTL and ETL) and the central emissive layer (EML). The EML material presents a 0.2 eV energy barrier for hole and electron injection from the corresponding

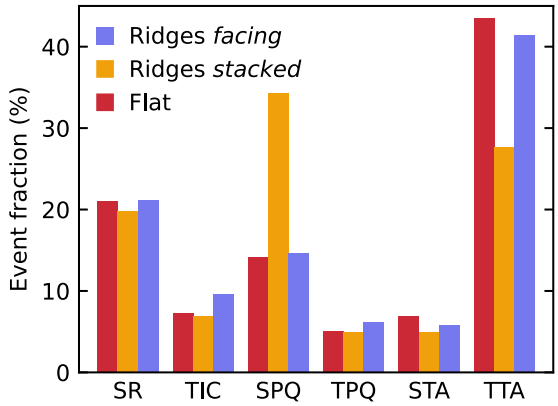

FIG. 9. Bipolar three layers, loss processes. Comparison of excitonic events in three-layer devices containing a flat interface or a ridges interface (20 nm high, 50 nm wide) either with stacked or facing offset, under 5.0 V applied bias. Abbreviations: SR, singlet radiative decay; TIC, triplet internal conversion; SPQ (TPQ), singlet (triplet) polaron quenching; STA (TTA), singlet (triplet) triplet annihilation. Blocking layers prevent carrier collection at the opposite electrode.

transport layers, which also serve as blocking layers for the opposite charge carriers by means of a 0.5 eV energy barrier. The blocking function of HTL and ETL is crucial to grant carrier confinement within the EML: we find exciton generation within the transport layers to prevail otherwise (see Supplemental Material [42], Figs. S17 and S18). With two ridges interfaces, multiple configurations are possible, depending on the lateral offset: as we employ periodic morphologies, we consider the extremes of in-phase (*stacked*) and out-of-phase (*facing*) offset [Fig. 1(e)].

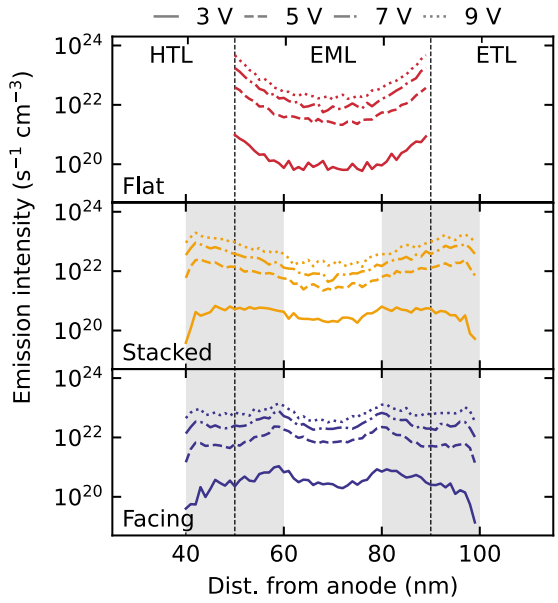

FIG. 10. Bipolar three layers, emission profiles. Emission profile in the anode-to-cathode direction for bipolar three layers containing a flat interface or a ridges interface 20 nm high, 50 nm wide either with stacked or facing offset. The dashed black lines indicate the position of the interfaces in the flat device. In the ridges devices, shadowed areas indicate regions where roughness implies EML- or transport-layer material may be present.

In Fig. 8, we consider how the width and offset of ridges morphologies affect the distribution of holes [Fig. 8(a)], singlet excitons [Fig. 8(b)], and the resulting exciton-polaron quenching [Fig. 8(c)] and exciton-exciton annihilation [Fig. 8(d)] events. The different loss processes (Fig. 9) and the emission profiles (Fig. 10) in a pair of ridges devices with different offset are finally compared against a flat device.

Figure 8(a) displays the hole distribution at a 5.0 V applied bias in ridges devices for two different aperture angles and for a stacked versus facing offset. As before, holes are funneled to the tips of the HTL-EML interface from where they are injected. This leads to inhomogeneous, quasifilamentary current flow with a charge shadowing effect in the areas between the tips. In both stacked and facing devices, holes accumulate inside the tips (i.e., in the concavities) of the EML-ETL interface as well. Similarly, by symmetry, electrons accumulate at the tips of the EML-ETL interface and in the valleys between the tips of the HTL-EML interface (see Supplemental Material [42], Fig. S15(a)). As a result, the electron and hole currents (indicated as white arrows in [Fig. 8(a)] are spatially separated in the stacked offset, while there is some overlap (in the neck between the tips) for a facing offset. The degree of overlap between the electron and hole current also depends on the feature size: it is larger for a 50 nm wide ridges morphology [bottom right of Fig. 8(a)] than for a 20 nm wide morphology [bottom left of Fig. 8(a)].

These filamentary currents determine the resulting singlet exciton distribution [Fig. 8(b)]. For the stacked offset, the scarce overlap between the hole and electron currents inside the EML results in exciton generation mainly in the concavities of the tips on either side of the EML, where electrons or holes accumulate. In contrast, for the facing offset, exciton generation is also strong in the crossover region of electron and hole current, i.e., at the narrow "necks" of the EML. The distribution for triplet excitons is similar, yet the excitons are more spread out due to the longer lifetime of the triplets, which allows for diffusion (see Supplemental Material [42], Fig. S15(b)). These sites of high charge and exciton density act as a hot spot for EPQ and EEA losses [respectively, Figs. 8(c) and 8(d)]. A detailed analysis in Fig. 9 shows that SPQ is the predominant loss mechanism for the ridges device with stacked offset, while TTA dominates in the flat device and in the ridges device with facing offset, in line with the observed distribution of charge and exciton density.

Consistent with the results for the bipolar bilayers, we find only minor differences in the IQE between the flat and ridges device. In fact, the devices with the facing offset and the flat devices give identical IQEs, and only those with the stacked offset are about 2% lower (see Supplemental Material [42], Fig. S19).

Even though the overall IQE hardly varies, we find that the presence of nanostructured interfaces between the transport and emissive layers leads to a conspicuous change in the emission profile along the anode-to-cathode axis. Figure 10 compares the emission profiles for the flat device and two ridges devices (20 nm high, 50 nm wide) with either stacked or facing offset. As the intensity is plotted against distance from

the anode, at some distance the charge transport layer extends into the EML and vice versa. In the flat device, the majority of radiative decay events happens within 7 nm from the HTL-ETL or ETL-EML interface. In the presence of two ridges interfaces, however, the emission profile is instead flattened out. The facing ridges devices presented in the bottom panel of Fig. 10 exhibit an almost flat emission profile scarcely affected by voltage. Further examples are given in Fig. S21 [42].

IV. DISCUSSION

To clarify the influence of rough interfaces within OLEDs, we have performed 3D-kinetic Monte Carlo simulations of ideal, symmetric bilayer and three-layer devices, both unipolar and bipolar, revealing that the microscopic behavior of a device can be significantly influenced by purely geometrical modifications of the interface morphology, namely, the introduction of rough features between adjacent layers. The presence of roughness considerably affects both charge and exciton dynamics in a shape- and size-dependent fashion. We shall first focus on the injection properties resulting from morphological variation.

In the presence of an energy barrier for charge transfer between layers, ridges morphologies (with triangular cross section) induce charge accumulation at the tips. The tips then act as injection points, determining the onset of quasifilamentary currents and leading to a strongly inhomogeneous distribution of charge carriers and excitons at the interface and in the adjacent layer. Ridges devices characteristically show enhanced charge injection across the energy barrier, yielding a significant rise in the current-voltage curve, compared to a flat-interface device. Conversely, devices containing a stripes morphology (with rectangular cross section) display negligible enhancement except at low voltage.

We attribute the increased current density through ridges devices to an enhanced carrier mobility at the tips, resulting from the locally larger charge density: higher occupation translates to a higher Fermi level, as visible from the occupied density of states (oDOS) at the tips in Fig. 11. We argue that the key difference between ridges and stripes devices is that, in ridges devices, the sloping interface allows charge carriers to "slide" alongside the interface: thus, both carrier drift and diffusion enable charge funneling toward a favorable injection point (i.e., the tip). Vice versa, in stripes devices, charge carriers meet a wall and need to diffuse in a direction parallel to its surface, in order to find a good spot to progress over the energy barrier or funnel forward into the stripes. This results in a weaker carrier funneling (further discussion is provided in the Supplemental Material [42], Sec. S5.2). The difference in carrier motion is clearly visible in the video provided as Supplemental Material [42]. The fact that downhill devices exhibit virtually no influence of the morphology on device behavior agrees well with this reasoning.

Consistently with the reasoning, equivalent morphologies in bipolar bilayer devices produce a smaller increase in current density [see Fig. 7(a)] compared to the flat device. The reason is that the recombination of charge carriers at the interfaces reduces the occupation at the tips [see Fig. 11(b)], thus producing a lower Fermi level. In contrast, in a three-layer structure, carrier recombination occurs in the central layer,

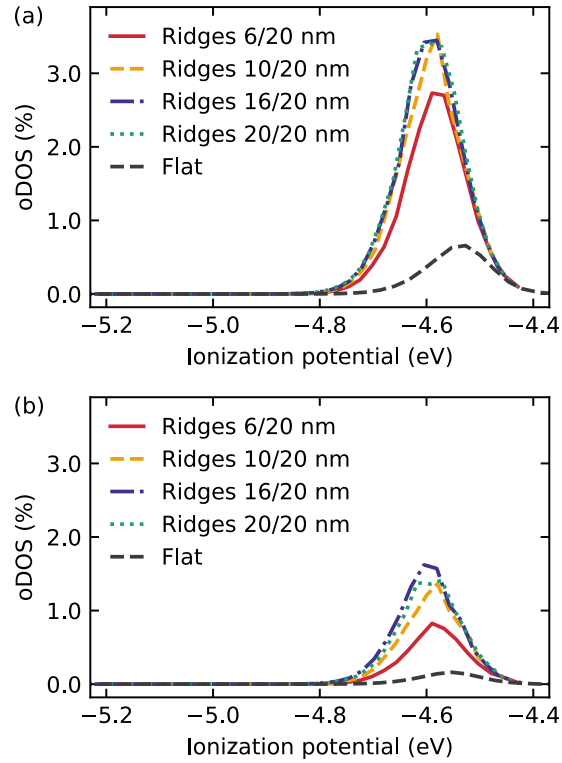

FIG. 11. oDOS. Occupied density of states at the tips of ridges interfaces in (a) unipolar or (b) bipolar uphill bilayer devices under 6.0 V bias. Devices contain a ridges interface 20 nm wide with varying height, as indicated. A flat device is reported for comparison.

and not at the tips of the charge injection layers [compare Fig. 5 versus Fig. 8(b)]. The charge carrier occupation at the tips remains high, thus preserving the injection boost that we reported for unipolar devices.

It is worth briefly mentioning that, in ridges devices, the Fermi level at the tips (E_F) strongly depends on the size of the ridges features, but such dependence cannot be tracked back to a universal trend with aperture angle α. Figure 11 reports the oDOS at the tips of ridges interfaces with varying sizes, in unipolar and bipolar devices. When the height is varied at constant width, DOS occupation increases, as charge funneling is more efficient. The dependence of tip occupation on aperture angle is detailed further in the Supplemental Material [42], Sec. S8 (including Refs. [48,49]).

We now consider the impact of interfacial morphology on emission. In bipolar devices with two and with three layers, we have observed a surprisingly minor impact of roughness on internal quantum efficiency (IQE) and IQE roll-off owing to a trade-off between loss mechanisms [Fig. 7(b)]. For the bilayer ridges devices, charge accumulation at the tip sites surprisingly does not increase exciton-polaron quenching (EPQ). We attribute this to the fact that a nominally flat interface and one with ridges resemble each other insofar, that for both interfaces, sites of high carrier density are also sites with a high probability for exciton formation, and hence for EPQ. Whether these sites are tail states in the DOS or geometric traps such as tips does not seem to matter much.

This is different for three-layer devices. The most noticeable difference is that, in three-layer devices, even for flat

interfaces the fraction of exciton-exciton annihilation events–more precisely, triplet-triplet annihilation (TTA)–increases drastically. In bilayer devices, TTA happens half as often as singlet-polaron quenching (SPQ), while in three-layer devices, TTA happens more than twice as often as SPQ (Figs. 6 and 9). The reason is that the sites of charge accumulation and exciton formation are separated in three-layer devices. High carrier densities only prevail in the charge transport layers. Once carriers enter the central emissive layer, they recombine to form excitons and are hence no longer present as charges. This is the case for the flat device and the ridges device with facing offset: sites of high carrier density are at the tips of the charge injection layer, while sites of high exciton density are at the same tips, yet inside the emissive layer, thus precluding strong SPQ. We recall the carrier pathways indicated by white arrows in Fig. 8(a) that result in efficient exciton formation at the necks, while charge accumulation, e.g., of holes, inside the EML only occurs comparatively weakly at the concave side of the tips, e.g., adjacent to the electron transport layer (ETL). For the stacked offset, however, this is different. Charges, e.g., holes, injected into the EML accumulate strongly at the concave tips to the next layer, e.g., the ETL [Fig. 8(a)]. These regions of charge accumulation are also the sites where excitons form [Fig. 8(b)], hence leading to a dominance of SPQ. The surprising feature is that this interplay between SPQ and TTA losses does not affect the overall emission efficiency, consistent with studies on simulated phosphorescent devices by van Eersel *et al.* [35].

Nevertheless, the three-layer structure can be used to fine tune the overlap between the hole and electron currents and thus to modulate the recombination zone inside the EML. As shown in Fig. 10, this can be used to achieve a surprisingly homogeneous, voltage-independent emission profile across the emissive layer. The disadvantage of such an approach is that increased carrier concentrations at tips can possibly enhance local degradation. Shen and Giebink [50] have associated filamentary charge transport with lifetime reduction in flat-interface simulated OLEDs similar to our model systems. Further simulations are, however, needed to verify whether the locally enhanced charge density and concentration of EPQ events in our model systems lead to a shorter device lifetime, compared to a flat-interface scenario where filamentary charge transport is rather caused by energetic disorder [51–53].

As a final note, our simulations could only explore morphologies up to a width scale of tens of nanometers, which is the upper threshold for state of the art kMC. Surface atomic force microscopy performed on as-deposited films [14,15,54–58] shows variations in film thickness usually of the order of 10 nm, but generally on a width scale of micrometers along the directions parallel to the electrodes. Such analysis may, however, reflect roughness arising from the substrate, reducing the effective thickness variations of internal layers. Nevertheless, we extrapolate from our simulations that, in the presence of corrugation on a large width scale, charge carrier funneling would be rather ineffective. Macroscopic effects such as the *JV* enhancement already vanish for a 20 nm high, 100 nm wide ridges morphology [Figs. 3(b) and 7(a)]. We emphasize that this 100 nm wide morphology still affects the microscopic behavior of the device by producing a visible inhomogeneity in charge distribution both in unipolar and bipolar uphill bilayers, displayed in Fig. 12.

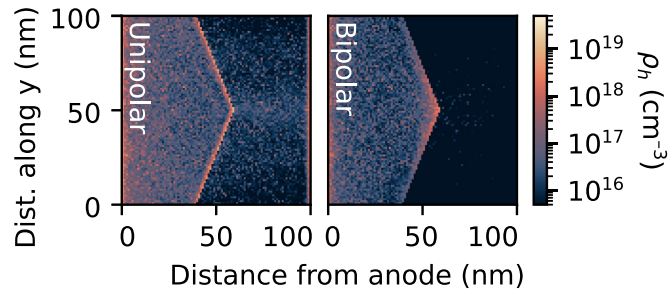

FIG. 12. Wide morphologies. Hole density maps at 6.0 V in a unipolar (left) or bipolar (right) uphill bilayer with a 20 nm high, 100 nm wide ridges morphology. Holes move from left to right.

V. CONCLUSIONS

We have employed three-dimensional kinetic Monte Carlo simulations of bi- and three-layer devices to elucidate the charge and exciton dynamics across rough organic-organic interfaces. We compared two interfacial morphologies with periodic corrugation and either rectangular (stripes) or triangular (ridges) cross section against a reference flat interface.

We detect significant impact of the interfacial morphology only when associated with an energy barrier for charge transport, in which case funneling of charge carriers to the tips of the interface creates an inhomogeneous distribution of charge density. Such funneling is favored in the presence of a ridges interface (particularly for smaller aperture angles). Significant inhomogeneities in charge and exciton density are present even for corrugations over a 100 nm width scale.

As the tips of the injection layer act as hot spots for charge injection, the current density of a ridges-interface device can be significantly enhanced compared to the reference flat-interface device, thus lowering the device operating voltage. Interfacial roughness does not affect the overall internal quantum efficiency of bi- and three-layer devices, although it favors exciton-polaron quenching losses over exciton-exciton annihilation processes. The interfacial morphology furthermore influences the recombination profile inside the emissive layer, yielding a flatter and less voltage-dependent profile compared to a flat-interface device.

On the downside, we draw attention to the possible role of roughness in aggravating device degradation due to the focusing of charge transport and losses in the tip volume, even when macroscopic properties such as the *JV* of the pristine device appear unaffected.

ACKNOWLEDGMENTS

G.C. wishes to thank Harm van Eersel for the technical support and Andrei Stankevych and Heinz Bässler for useful discussions. The authors acknowledge funding from the European Union Horizon 2021 research and innovation programme under Grant Agreement No. 101073045 (TADF-solutions).

G.C., A.K., and S.G. conceived the project. G.C. performed kMC simulations under the supervision of S.G., E.T., and A.K. G.C., and A.K. wrote the paper with input from all authors.

The authors declare no competing interests.

DATA AVAILABILITY

The data that support the findings of this article are not publicly available. The data are available from the authors upon reasonable request.

[1] F. Villani, P. Vacca, G. Nenna, O. Valentino, G. Burrasca, T. Fasolino, C. Minarini, and D. Della Sala, Inkjet printed polymer layer on flexible substrate for OLED applications, J. Phys. Chem. C **113**, 13398 (2009).

[2] C. Zhong, C. Duan, F. Huang, H. Wu, and Y. Cao, Materials and devices toward fully solution processable organic light-emitting diodes, Chem. Mater. **23**, 326 (2011).

[3] A. Verma, D. M. Zink, C. Fléchon, J. Leganés Carballo, H. Flügge, J. M. Navarro, T. Baumann, and D. Volz, Efficient, inkjet-printed TADF-OLEDs with an ultra-soluble NHetPHOS complex, Appl. Phys. A **122**, 191 (2016).

[4] A. C., B. Luszczynska, M. Z. Szymanski, J. Ulanski, K. Albrecht, and K. Yamamoto, Inkjet printing of thermally activated delayed fluorescence (TADF) dendrimer for OLEDs applications, Org. Electron. **74**, 218 (2019).

[5] J. Y. Woo, M. Park, S. Jeong, Y. Kim, B. Kim, T. Lee, and T. Han, Advances in solution-processed OLEDs and their prospects for use in displays, Adv. Mater. **35**, 2207454 (2022).

[6] X.-Y. Zeng, Y.-Q. Tang, X.-Y. Cai, J. Tang, and Y. Li, Solution-processed OLEDs for printing displays, Mater. Chem. Front. **7**, 1166 (2023).

[7] T. Lee, T. Noh, H. Shin, O. Kwon, J. Park, B. Choi, M. Kim, D. W. Shin, and Y. Kim, Characteristics of solution-processed small-molecule organic films and light-emitting diodes compared with their vacuum-deposited counterparts, Adv. Funct. Mater. **19**, 1625 (2009).

[8] L. Duan, L. Hou, T.-W. Lee, J. Qiao, D. Zhang, G. Dong, L. Wang, and Y. Qiu, Solution processable small molecules for organic light-emitting diodes, J. Mater. Chem. **20**, 6392 (2010).

[9] F. Samaeifar and H. Aziz, The root causes of the limited electroluminescence stability of solution-coated versus vacuum-deposited small-molecule OLEDs: A mini-review, Front. Chem. **10**, 857551 (2022).

[10] Y. J. Cho, Y. Zhang, H. Yu, and H. Aziz, The root causes of the limited stability of solution-coated small-molecule organic light-emitting devices: Faster host aggregation by exciton–polaron interactions, Adv. Funct. Mater. **26**, 8662 (2016).

[11] H. Yu and H. Aziz, Differences in photoluminescence stability and host-to-guest energy transfer in solution-coated versus vacuum-deposited electroluminescent host: Guest small-molecule materials, J. Phys. Chem. C **124**, 11701 (2020).

[12] F. Samaeifar and H. Aziz, Role of guest materials in the lower stability of solution-coated versus vacuum-deposited phosphorescent oleds, ACS Appl. Mater. Interfaces **14**, 8199 (2022).

[13] M. Shibata, Y. Sakai, and D. Yokoyama, Advantages and disadvantages of vacuum-deposited and spin-coated amorphous organic semiconductor films for organic light-emitting diodes, J. Mater. Chem. C **3**, 11178 (2015).

[14] V. N. Hamanaka, E. Salsberg, F. J. Fonseca, and H. Aziz, Investigating the influence of the solution-processing method on the morphological properties of organic semiconductor films and their impact on OLED performance and lifetime, Org. Electron. **78**, 105509 (2020).

[15] G. Mao, Z. Wu, Q. He, B. Jiao, G. Xu, X. Hou, Z. Chen, and Q. Gong, Considerable improvement in the stability of solution processed small molecule OLED by annealing, Appl. Surf. Sci. **257**, 7394 (2011).

[16] S. Feng, L. Duan, L. Hou, J. Qiao, D. Zhang, G. Dong, L. Wang, and Y. Qiu, A comparison study of the organic small molecular thin films prepared by solution process and vacuum deposition: Roughness, hydrophilicity, absorption, photoluminescence, density, mobility, and electroluminescence, J. Phys. Chem. C **115**, 14278 (2011).

[17] K. M. Kuznetsov, M. I. Kozlov, A. N. Aslandukov, A. A. Vashchenko, A. V. Medved'ko, E. V. Latipov, A. S. Goloveshkin, D. M. Tsymbarenko, and V. V. Utochnikova, $Eu(tta)_3$ DPPZ-based organic light-emitting diodes: Spin-coating vs. vacuum-deposition, Dalton Trans. **50**, 9685 (2021).

[18] S. S. Chang, A. B. Rodríguez, A. M. Higgins, C. Liu, M. Geoghegan, H. Sirringhaus, F. Cousin, R. M. Dalgleish, and Y. Deng, Control of roughness at interfaces and the impact on charge mobility in all-polymer field-effect transistors, Soft Matter **4**, 2220 (2008).

[19] Y. Wang and X. Zhan, Layer-by-layer processed organic solar cells, Adv. Energy Mater. **6**, 1600414 (2016).

[20] K. Nakano and K. Tajima, Organic planar heterojunctions: From models for interfaces in bulk heterojunctions to high-performance solar cells, Adv. Mater. **29**, 1603269 (2017).

[21] K. Matsuoka, K. Albrecht, A. Nakayama, K. Yamamoto, and K. Fujita, Highly efficient thermally activated delayed fluorescence organic light-emitting diodes with fully solution-processed organic multilayered architecture: Impact of terminal substitution on carbazole–benzophenone dendrimer and interfacial engineering, ACS Appl. Mater. Interfaces **10**, 33343 (2018).

[22] F. Fischer, T. Hahn, H. Bässler, I. Bauer, P. Strohriegl, and A. Köhler, Measuring reduced C_{60} diffusion in crosslinked polymer films by optical spectroscopy, Adv. Funct. Mater. **24**, 6172 (2014).

[23] C. Saller, F.-J. Kahle, T. Müller, T. Hahn, S. Tscheuschner, D. Priadko, P. Strohriegl, H. Bässler, and A. Köhler, Facile method for the investigation of temperature-dependent C_{60} diffusion in conjugated polymers, ACS Appl. Mater. Interfaces **10**, 21499 (2018).

[24] J. A. McEwan, A. J. Clulow, A. Nelson, A. M. Krause-Heuer, R. D. Jansen-van Vuuren, P. L. Burn, and I. R. Gentle, Diffusion in organic film stacks containing solution-processed phosphorescent poly(dendrimer) dopants, ACS Appl. Mater. Interfaces **13**, 30910 (2021).

[25] Ch. Jonda, A. B. R. Mayer, U. Stolz, A. Elschner, and A. Karbach, Surface roughness effects and their influence on the

degradation of organic light emitting devices, J. Mater. Sci. **35**, 5645 (2000).

[26] Y.-H. Tak, K.-B. Kim, H.-G. Park, K.-H. Lee, and J.-R. Lee, Criteria for ITO (indium–tin-oxide) thin film as the bottom electrode of an organic light emitting diode, Thin Solid Films **411**, 12 (2002).

[27] M.-C. Sun, J.-H. Jou, W.-K. Weng, and Y.-S. Huang, Enhancing the performance of organic light-emitting devices by selective thermal treatment, Thin Solid Films **491**, 260 (2005).

[28] B. Riedel, I. Kaiser, J. Hauss, U. Lemmer, and M. Gerken, Improving the outcoupling efficiency of indium-tin-oxide-free organic light-emitting diodes via rough internal interfaces, Opt. Express **18**, A631 (2010).

[29] G. A. Buxton and N. Clarke, Computer simulation of polymer solar cells, Modell. Simul. Mater. Sci. Eng. **15**, 13 (2007).

[30] P. K. Watkins, A. B. Walker, and G. L. B. Verschoor, Dynamical Monte Carlo modelling of organic solar cells: The dependence of internal quantum efficiency on morphology, Nano Lett. **5**, 1814 (2005).

[31] BUMBLEBEE is currently provided by SCM, Amsterdam, The Netherlands, https://www.scm.com/oled/oled-workflows (2024).

[32] H. van Eersel, P. A. Bobbert, R. A. J. Janssen, and R. Coehoorn, Monte Carlo study of efficiency roll-off of phosphorescent organic light-emitting diodes: Evidence for dominant role of triplet-polaron quenching, Appl. Phys. Lett. **105**, 143303 (2014).

[33] R. Coehoorn, H. van Eersel, P. Bobbert, and R. Janssen, Kinetic Monte Carlo study of the sensitivity of OLED efficiency and lifetime to materials parameters, Adv. Funct. Mater. **25**, 2024 (2015).

[34] A. Ligthart, X. de Vries, L. Zhang, M. C. W. M. Pols, P. A. Bobbert, H. van Eersel, and R. Coehoorn, Effect of triplet confinement on triplet-triplet annihilation in organic phosphorescent host-guest systems, Adv. Funct. Mater. **28**, 1804618 (2018).

[35] H. van Eersel, P. A. Bobbert, R. A. J. Janssen, and R. Coehoorn, Effect of Förster-mediated triplet-polaron quenching and triplet-triplet annihilation on the efficiency roll-off of organic light-emitting diodes, J. Appl. Phys. **119**, 163102 (2016).

[36] M. Mesta, H. van Eersel, R. Coehoorn, and P. A. Bobbert, Kinetic Monte Carlo modeling of the efficiency roll-off in a multilayer white organic light-emitting device, Appl. Phys. Lett. **108**, 133301 (2016).

[37] S. Gottardi, M. Barbry, R. Coehoorn, and H. van Eersel, Efficiency loss processes in hyperfluorescent OLEDs: A kinetic Monte Carlo study, Appl. Phys. Lett. **114**, 073301 (2019).

[38] C. Hauenstein, S. Gottardi, E. Torun, R. Coehoorn, and H. van Eersel, Identification of OLED degradation scenarios by kinetic Monte Carlo simulations of lifetime experiments, Front. Chem. **9**, 823210 (2022).

[39] M. Mesta, M. Carvelli, R. J. de Vries, H. van Eersel, J. J. M. van der Holst, M. Schober, M. Furno, B. Lüssem, K. Leo, P. Loebl, R. Coehoorn, and P. A. Bobbert, Molecular-scale simulation of electroluminescence in a multilayer white organic light-emitting diode, Nat. Mater. **12**, 652 (2013).

[40] H. van Eersel, Device physics of organic light-emitting diodes: Interplay between charges and excitons, Ph.D. thesis, Technische Universiteit Eindhoven, 2015.

[41] H. Bässler, Charge transport in disordered organic photoconductors a Monte Carlo simulation study, Phys. Status Solidi B **175**, 15 (1993).

[42] See Supplemental Material at http://link.aps.org/supplemental/10.1103/36kq-7pvt for a detailed description of methods and further results.

[43] J. J. M. van der Holst, F. W. A. van Oost, R. Coehoorn, and P. A. Bobbert, Monte Carlo study of charge transport in organic sandwich-type single-carrier devices: Effects of Coulomb interactions, Phys. Rev. B **83**, 085206 (2011).

[44] K. Zojer, Simulation of charge carriers in organic electronic devices: Methods with their fundamentals and applications, Adv. Opt. Mater. **9**, 2100219 (2021).

[45] F. Crameri, Scientific colour maps (2023), https://zenodo.org/record/1243862.

[46] S. L. M. Van Mensfoort, V. Shabro, R. J. De Vries, R. A. J. Janssen, and R. Coehoorn, Hole transport in the organic small molecule material α-NPD: Evidence for the presence of correlated disorder, J. Appl. Phys. **107**, 113710 (2010).

[47] H. Yoshida and K. Yoshizaki, Electron affinities of organic materials used for organic light-emitting diodes: A low-energy inverse photoemission study, Org. Electron. **20**, 24 (2015).

[48] T. Meier, Modellierung von ladungstransport in organischen feldeffekttransistoren mittels eines kinetischen Monte-Carlo-Ansatzes, Ph.D. thesis, University of Bayreuth, 2023.

[49] W. Li and H. Kwok, Conduction mechanisms in organic semiconductors, in *Encyclopedia of Nanotechnology*, edited by B. Bhushan (Springer Netherlands, Dordrecht, 2012), pp. 493–500.

[50] Y. Shen and N. C. Giebink, Monte Carlo simulations of nanoscale electrical inhomogeneity in organic light-emitting diodes and its impact on their efficiency and lifetime, Phys. Rev. Appl. **4**, 054017 (2015).

[51] E. Tutiš, I. Batistić, and D. Berner, Injection and strong current channeling in organic disordered media, Phys. Rev. B **70**, 161202(R) (2004).

[52] J. J. M. van der Holst, M. A. Uijttewaal, B. Ramachandhran, R. Coehoorn, P. A. Bobbert, G. A. de Wijs, and R. A. de Groot, Modeling and analysis of the three-dimensional current density in sandwich-type single-carrier devices of disordered organic semiconductors, Phys. Rev. B **79**, 085203 (2009).

[53] R. Coehoorn and P. A. Bobbert, Effects of Gaussian disorder on charge carrier transport and recombination in organic semiconductors: Charge carrier transport and recombination in organic semiconductors, Phys. Status Solidi A **209**, 2354 (2012).

[54] W. H. Kim, G. P. Kushto, H. Kim, and Z. H. Kafafi, Effect of annealing on the electrical properties and morphology of a conducting polymer used as an anode in organic light-emitting devices, J. Polym. Sci. Part B: Polym. Phys. **41**, 2522 (2003).

[55] P. Wilson, C. Lekakou, and J. F. Watts, A comparative assessment of surface microstructure and electrical conductivity dependence on co-solvent addition in spin coated and inkjet printed poly(3,4-ethylenedioxythiophene): Polystyrene sulphonate (PEDOT:PSS), Org. Electron. **13**, 409 (2012).

[56] Y. Yoon, H. Lee, T. Kim, K. Kim, S. Choi, H. K. Yoo, B. Friedman, and K. Lee, Post-annealing effect on the interface morphology and current efficiency of organic light-emitting diodes, Solid State Electron. **79**, 45 (2013).

[57] Y. J. Cho, K. S. Yook, and J. Y. Lee, High efficiency in a solution-processed thermally activated delayed-fluorescence device using a delayed-fluorescence emitting material with improved solubility, Adv. Mater. **26**, 6642 (2014).

[58] C. Zhang, H. Yan, Y. He, Y. Chai, and D. Zhou, Thermally activated delayed fluorescence dendrimers achieving 20% external quantum efficiency for solution-processed OLEDs, Mater. Chem. Front. **6**, 3442 (2022).